Available online at www.sciencedirect.com
SCIENCE DIRECT®
Planetary and Space Science 52 (2004) 1233–1249
Planetary and Space Science
www.elsevier.com/locate/pss

Semianalytic theory of motion for close-Earth spherical satellites including drag and gravitational perturbations

A. Bezděk[a,*], D. Vokrouhlický[b]

[a] *Astronomical Institute, Academy of Sciences of the Czech Republic, Fričova 298, 251 65 Ondřejov, Czech Republic*
[b] *Institute of Astronomy, Charles University, V Holešovičkách 2, 180 00 Prague 8, Czech Republic*

Received 26 April 2004; received in revised form 29 June 2004; accepted 25 August 2004

Abstract

A semianalytic theory for long-term dynamics of a low Earth orbit artificial satellite, or a space debris particle, is presented. The empirical model TD88 of the neutral atmosphere density distribution, simple enough to allow analytic removal of short period perturbations, is the principal part of the theory. In order to compare our results with observations of passive spherical bodies, we also include the main gravitational effects, notably those of the zonal harmonics $J_2, \ldots, J_9$ (J_2^2 terms are also considered), and for low eccentricities and inclinations we use the description in nonsingular elements. Starting with a single set of initial orbital data and giving a certain "confidential interval" on the resulting lifetimes, we find a reasonably good agreement with observations over the timescale of years, the mean computed lifetimes being a few percent apart from the real ones. The strength of our theory is the computational efficiency, since we need only $\simeq 5$ s (on a PC equipped with Intel Celeron 1.7 GHz) to propagate the 10-year orbital arc, while maintaining a lot of the physics of the motion under drag (solar flux, geomagnetic activity, local time, geographic latitude). The online calculation as well as the code are available on the internet.

PACS: 91.10.Sp; 95.40.+s

Keywords: LEO satellites; Atmospheric drag; Space debris; Satellite lifetimes

1. Introduction

The problem of the orbital motion of celestial bodies in a resistive medium can be traced back to Newton's Principle (Newton, 1687, bk. II, Sec. I–IV) and Laplace's analysis of a possibly finite velocity of gravitation (Laplace, 1805). However, with the advent of the space age there arose the need of precisely predicting the orbital behaviour of the newly launched bodies. Compared to the gravitational perturbations, the adequate allowance for atmospheric drag turned out to be a problem for unforeseen complexity (Brouwer, 1963). Besides the obstacles in the analytical treatment of the drag based on the idealized spherical nonrotating density model, the upper atmosphere revealed itself to behave unexpectedly. The irregular density variations derived from orbital analyses of the first launched satellites were attributed to the influence of the Sun, as they displayed periodical changes of approximately 27 days. In December 1958 this conjecture was most persuasively confirmed by the juxtaposition of the density variations and those of the measured centimetre solar radio flux. Another clue pointing to the "solar-radiation hypothesis" was the overall dependence of the drag on the angle between the perigee and the Sun (Jacchia, 1959a; King-Hele and Walker, 1959). In the subsequent years, together with the advances in theory (King-Hele, 1964), direct evidence has grown that the

*Corresponding author. Tel.: +420 323620232.
E-mail addresses: bezdek@asu.cas.cz (A. Bezděk), vokrouhl@cesnet.cz (D. Vokrouhlický).
URLS: http://www.asu.cas.cz/~bezdek/density_therm/pohtd/, http://astro.mff.cuni.cz/davok/.

0032-0633/$ - see front matter © 2004 Elsevier Ltd. All rights reserved.
doi:10.1016/j.pss.2004.08.004

solar and geomagnetic effects stronglyinfluence the thermospheric density at a variety of timescales, both periodically and randomly (Jacchia, 1959b, 1960, 1961, Jacchia and Slowey, 1962a,b). In order to accurately describe a satellite's motion through the thermosphere over a long period of time, one has to take these effects into account, apart from the obvious quasi-exponential decrease of density with height.

Beginning in the 1960s the ground-based or in situ data deduced from mass spectrometers, accelerometers, optical techniques, and incoherent scatter radar measurements were extensive enough to construct more detailed models of the upper atmosphere. The physical models of the thermosphere and derived from the a priori known physical laws and try to reproduce the variations in the measured values. Such a goal is extremely ambitious and is still not achieved for the operational use of such models in predicting the motion of artificial satellites. Semiempirical models based on simplified physical concepts proved to be more successful in representing the observed thermospheric density variations, starting with the 1965 Jacchia model (Barlier and Berger, 1983; Marcos, 2002; Lathuillère et al., 2002). The widely used semiempirical model series such as Jacchia (Jacchia, 1964, 1970, 1971, 1977), DTM (Barlier et al., 1978; Berger et al., 1998) or MSIS (Hedin, 1983, 1987, 1991; Picone et al., 2002) combine some simplified physical hypotheses, e.g.,, static diffusive equilibrium of the different thermospheric constituents above the heterosphere base, with the fitting on the measured data. Finally, there existpurely empirical models of the thermospheric density that are based on fitting the semiempirical models with the aim of the maximum computational speed (e.g., de Lafontaine and Hughes, 1983; Gill, 1996).

Although the semiempirical models are physically simplified, they do not permit the analytical solution of the equations of motion. Representing the state-of-the-art description of the thermospheric density variations, the semiempirical models are used in predicting the satellite behaviour on short-term periods typically up to several days by means of numerical integration. However, for long-term satellite dynamics, lifetime predictions, fuel consumption planning, one has also needed to know the evolution of satellite orbits over longer time spans. Over the years a lot of long-term analytical or semianalytic motion theories expressing the atmospheric drag for LEO satellites by substantially simplified density models have been developed. The semianalytic theory summarized in the classical book by King-Hele (1964) makes use of the oblate rotating thermosphere with the altitude-dependent scale height to find the drag induced changes over one satellite revolution. The SGP4 orbit propagator with a power density function is widely used in connection with the NORAD two-line element sets (Hoots and Roehrich, 1980). For discussion of the numerical and analytical approaches to modelling the satellite motion see e.g., Gooding (1981), Fonte et al. (1995), Hoots and France (1997).

The idea behind the construction of the TD88 model of the thermospheric density (Sehnal, 1988, 1990b; Sehnal and Pospíšilová, 1988) and thereto related theory of motion (Sehnal, 1990a), was to develop a new kind of semianalytic theory of the LEO satellite motion under the influence of air drag. In contrast to other semianalytic theories with static atmospheric density models, the TD88 model explicitly includes dependence on the physical parameters dynamically influencing the air density (solar flux, geomagnetic index, local time, day of year, latitude). TD88 is an empirical density model with numerical coefficients determined by fitting the TD88 densities to the satellite drag data and the DTM78 model values (Barlier et al., 1978) within the height range of 150–750 km. The TD88 density model can be analytically integrated over one revolution of the satellite, thus defining the least time step of the theory. With the dynamical reaction of the atmospheric drag on the changing physical conditions, the TD88 theory is able to predict the motion of the satellite over long time spans, starting with only one set of initial orbital data. This is a rather unique feature, since other semianalytic theories usually extrapolate the recent changes in orbital elements due to the drag neglecting the fluctuating physical state of the thermosphere with the risk of a drag induced positional error propagating further on. In a somewhat similar way to the TD88 theoryHoots and France (1987) and Danielson et al. (1995) use the drag effects given by a dynamical thermospheric model, but conveniently numerically integrated over one revolution. Given the purely empirical approach, the TD model can be used to compute density at a particular space and time location nearly an order of magnitude faster than the semiempirical models such as DTM or MSIS. For that reason Montenbruck and Gill (2001) characterize the TD model as extremely rapid; on the other hand, they find it also of a very low accuracy. However, we think that methodology by which they reach this conclusion is incorrect, in fact, the TD88 model is of comparable accuracy as other models of thermospheric density within its proper height range, and it is suitable for a rapid description of the long-term orbital evolution as demonstrated below.

Helali (1987) was the first who used the TD model to obtain a semianalytic prediction of the perigee-height evolution. However, his analysis was incomplete since he omitted two, computationally most difficult terms in the TD density formulation (notably the diurnal terms (6)). Similarly, Šegan (1988) making use of the algebra manipulation program obtained orbit-averaged variations of the semimajor axis and the eccentricity using the TD model, but he limited his formulation to the case of zero-eccentricity orbits; with this he compared the

theory and observations of Intercosmos 10 (1973-82A) satellite and concluded 'some differences persist, perhaps due to incompleteness of the model'. Another attempt to use the TD model for a fast orbit propagation was the work of Sehnal and Pospíšilová (1991) (see also Sehnal, 1990a), who determined lifetime of the satellite Rohini 1 (1980-62B). Rossi et al. (1998) used a substantially simplified version of the TD model to simulate the thermospheric drag effects on the long-term behaviour of space debris population around the Earth.

The aim of this paper is to present a new, extended implementation of the TD88 drag theory and to discuss how its theoretical predictions compare with the orbital data of several real-world artificial satellites. In addition to the variations in the semimajor axis and eccentricity (Sehnal, 1990a), we include the perturbations in the inclination which reflect the net thermospheric rotation with respect to the Earth surface. Because of the tendency to circularize the orbits, and in order to treat orbits with initially small eccentricity, we pay a special attention to this limit. Notably, a formulation in nonsingular elements is used for these cases (which introduces the drag effects on the argument of perigee). A complete description of the satellite motion requires consideration other than atmospheric effects; in this paper we restrict ourselves to the effects of the geopotential zonal harmonics, nevertheless, weaker effects may be included in a straightforward way. As part of our work, we also extended altitude range of applicability of the TD model to 1200 km (Appendix B).

When dealing with atmospheric drag acting on LEO satellites, one of the important sources of uncertainty is the drag coefficient C_D. Here our method is to make a "lifetime prediction" for each satellite as though we were at the moment of its launch and we got the initial set of its orbital elements. To be able to compare the TD88 density model with reality, we assume that we know the solar and geomagnetic conditions during the flight. Further, we suppose a perfect knowledge of the mass and diameter of each satellite, the uncertainties or small variations in these parameters being included in the overall uncertainty of the drag coefficient. Even if we confine ourselves to spherical satellites, there is still not a generally accepted model for their C_D. This choice of the interval $C_D \in \langle 2.09; 2.31\rangle$, within which we suppose the actual C_D lies for the satellites below, say, 500 km, is in agreement with the range of the C_D values given by the recent theoretical models of C_D based on the molecule-surface interactions data measured at satellite heights (it should be mentioned, however, that C_D generally increases with height, see Section 2.1.2)(Moe et al., 1993, 1996, 1998). The output of the presented theory is a time interval, within which the real lifetime should fall—we may regard it as a "C_D-based confidential interval" of the calculated lifetime. For convenience, in figures we sometimes draw a curve denoted as "best-fit C_D", which was found by fitting the computed time of flight to the actual lifetime.

For the development of the defining formulæ of the theory to the final complex expressions and for their subsequent export into the Fortran 77 code the computer system Maple 8 was used. The code of the theory is available on the internet (http://www.asu.cas.cz/~bezdek/density_therm/pohtd/), as well as the online computation for a desired real or fictitious LEO body.

2. Theory

In this section, we summarize the orbital perturbations taken into account in this work. The principal element here is a semianalytic treatment of the atmospheric drag effects (Section 2.1), whose primary limitation is the assumption of spherical shape of the satellite. In order to compare our results with observations, we complement the atmospheric effects with the main gravitational perturbations, notably those from the zonal harmonics of the geopotential (Section 2.2). Effects of finer substance, such as the tesseral harmonics (e.g., Kaula, 1966; Deleflie et al., 2004a, b), lunisolar perturbations (e.g., Kozai, 1973; Giacaglia, 1973), tidal effects (e.g., Musen, 1961; Casotto, 1991) or radiation pressure (e.g., Milani et al., 1987), can be implemented too. We linearly superimpose first-order contributions of different effects, except for the J_2 perturbation that is treated to the second-order, with no attempt to analytically couple drag effects with gravitational perturbations (see e.g., Brouwer and Hori, 1961; Delhaise, 1991). Though such a coupling is of theoretical interest by its subtlety, the primary uncertainty of models aiming to propagate satellite orbits in the thermosphere over long period of time arises due to mismodelling of the physical, mostly irregular phenomena related to solar and geomagnetic activity (see e.g., Fig. 3). We also note that a more straightforward method of coupling various perturbing effects together is to numerically integrate the averaged Lagrange or Gauss equations, such as in Breiter and Métris (1999), however this is not considered here.

2.1. Atmospheric drag

We first briefly review the TD model (Sehnal, 1988, 1990b; Sehnal and Pospíšilová, 1991) and outline the method used to obtain the long-term perturbations of semimajor axis, eccentricity and inclination; the angular orbital elements are not considered except for the argument of perigee in the small eccentricity limit.

2.1.1. Thermospheric density model TD

Thermospheric density ρ depends in a complex way on a variety of parameters, fundamental of which are: (i) the altitude h above the geoid, describing its vertical structure, (ii) the geographic latitude ϕ and longitude λ, related to direction towards specific energy sources such as the Sun or polar regions, and (iii) their numerous regular and irregular features in time. Characteristic to the vertical structure is the exponential decrease with a scale height H, that however itself depends on the altitude, in this way reflecting composition variations and other physical phenomena. Angular density dependence is usually expressed in terms of development in spherical functions with the symmetry axis oriented toward the energy source, and the temporal variability reflects principally local solar time, solar and geomagnetic activity. The TD model as an empirical model defines the thermospheric density as

$$\rho = f_x f_0 k_0 \sum_{n=1}^{7} g_n h_n, \tag{1}$$

where

$$f_x = 1 + a_1(F_x - F_b), \tag{2a}$$

$$f_0 = a_2 + f_m, \tag{2b}$$

$$k_0 = 1 + a_3(K_p - 3), \tag{2c}$$

$$f_m = (F_b - 60)/160, \tag{2d}$$

functions take into account variable solar and geomagnetic effects: F_x is the solar radio flux at 10.7 cm wavelength for a previous day and F_b its mean value over 81 days (three solar rotations), both given in $10^{-22}\,\mathrm{W\,m^{-2}\,Hz^{-1}}$, and K_p is the appropriate geomagnetic index 3 h before the date. Flare-induced irregular increase of the solar activity, and related major disturbances of the geomagnetic field, are thus translated into the thermospheric density. These are by far the most important stochastic effects which need to be included in a dynamic drag model (see e.g., Fig. 3).

Vertical density variations are approximated with a sum of exponentials

$$h_n = K_n + \sum_{j=1}^{3} K_{nj} \exp\left(\frac{\bar{h} - h}{jH}\right), \tag{3}$$

having scale heights multiples of the fundamental value 29 km (Sehnal, 1990b). The reference altitude, roughly corresponding to the heterosphere base is $\bar{h} = 120$ km.

Angular dependence and, mostly regular, variability in time are given by the functions g_n in (1). The constant and solar cycle parts are

$$g_1 = 1, \tag{4a}$$

$$g_2 = f_m/2 + a_4, \tag{4b}$$

while the annual and semiannual effects are

$$g_3 = (1 + a_5 f_m)\sin 2(d - p_4), \tag{5a}$$

$$g_4 = (1 + a_6 f_m)\sin(d - p_5), \tag{5b}$$

$$g_5 = \sin(d - p_3)\sin\phi, \tag{5c}$$

here d is the day count in the year. The short-period terms correspond to the diurnal and semidiurnal variations

$$g_6 = (1 + a_7 f_m)\sin(t - p_6)\cos\phi, \tag{6a}$$

$$g_7 = (1 + a_8 f_m)\sin 2(t - p_7)\cos^2\phi, \tag{6b}$$

with t denoting the local solar time. These terms approximate a lagged atmospheric bulge in the solar direction.

The model is numerically determined by a set of constants H, a_n ($n = 1,\ldots,8$), K_n and K_{nj} ($n = 1,\ldots,7$ and $j = 1,\ldots,3$), and phases p_i ($i = 3,\ldots,7$). By fitting TD model density predictions to observations and those of the DTM78 model, Sehnal (1988, 1990b) and Sehnal and Pospíšilová (1988) derived (a_n, K_n, K_{nj}, p_i) suitable for the height range 150–750 km; see Appendix A. To allow higher satellite orbits, we obtained another set of constants $(H, a_n, K_n, K_{nj}, p_i)$ appropriate for the height range 750–1200 km; see Appendix B.

2.1.2. Orbital perturbations

Consider a spherical satellite moving through a resistive medium, such as the thermosphere, and denote its relative velocity with respect to the rest frame by $\mathbf{V}$. In the free molecular flow regime (rarefied gas of noninteracting particles with long mean free path), the satellite experiences drag given by (Sterne, 1960; King-Hele, 1964; Fitzpatrick, 1970)

$$\mathbf{f} = -\frac{C_\mathrm{D}}{2}\frac{S}{m}\rho V\mathbf{V}, \tag{7}$$

where S is the satellite cross-section, m its mass, ρ the thermospheric density and C_D a drag coefficient. The latter depends in a complicated way on (i) microphysics of particle interaction with the satellite surface, and (ii) the ratio of the particles' thermal speed and V (expressed usually as series in this parameter; e.g., Zarrouati, 1987; Milani et al., 1987). A typical value for low altitude satellites is $C_\mathrm{D} \simeq 2.2$ while at higher altitudes C_D increases (in part due to the composition variations and also due to higher thermal velocity of atmospheric constituents). To keep things simple, in this paper we assume C_D to be constant, but an adjustable parameter for each satellite.

Since the thermosphere is not stationary in the inertial frame, but rather rotates with an angular velocity $\boldsymbol{\omega}_t$, we have $\mathbf{V} = \mathbf{v} - \boldsymbol{\omega}_t \times \mathbf{r}$, where $(\mathbf{r}, \mathbf{v})$ are the satellite geocentric position vector and orbital velocity. As mentioned below, the appropriate value of $\boldsymbol{\omega}_t$ is a

delicate issue, and we again start with the simplest model of the thermosphere corotating with the Earth. We denote

$$\delta = C_{\mathrm{D}} \frac{S}{m}, \tag{8a}$$

$$\tau = \frac{\omega_t}{n}\, \eta \cos I, \tag{8b}$$

where n is the satellite's mean motion, I the inclination of its orbit and $\eta^2 = 1 - e^2$ (e is the orbital eccentricity). With these parameters, we obtain

$$T = -\frac{\delta}{2}\, \rho v^2 \mathscr{B}^2, \tag{9a}$$

$$N = -\frac{\delta}{2}\, \rho v^2\, \frac{e\tau}{\eta}\, \mathscr{B}\, \frac{F_-}{F_+} \sin E, \tag{9b}$$

$$W = -\frac{\delta}{2}\, \rho v^2\, \frac{\tau \tan I}{\eta}\, \mathscr{B} F_- \sqrt{\frac{F_-}{F_+}} \cos \zeta, \tag{9c}$$

for the acceleration component T along the tangent of the orbit, and parallel with $\mathbf{v}$, the component N normal to the tangent and directed away from the centre, and the component W perpendicular to the precedent ones; for convenience we introduced $F_\pm(E) = 1 \pm e \cos E$, where E is the osculating eccentric anomaly, $\mathscr{B} = 1 - \tau F_-/F_+$ and $\zeta = \omega + f$, where f is the true anomaly and ω is the argument of perigee. Inserting (9a) in Gauss equations, we obtain (compare with results by King-Hele, 1964 or Fitzpatrick, 1970)

$$\frac{\mathrm{d}a}{\mathrm{d}E} = -a^2 \rho \delta \Sigma_a, \tag{10a}$$

$$\frac{\mathrm{d}e}{\mathrm{d}E} = -a \rho \delta \Sigma_e, \tag{10b}$$

$$\frac{\mathrm{d}I}{\mathrm{d}E} = -a \rho \delta\, \frac{\tau \tan I}{2\eta^2}\, \Sigma_I, \tag{10c}$$

for the rate of change of the osculating semimajor axis a, eccentricity e and inclination I. Here, we have

$$\Sigma_a = \mathscr{B}^2 F_+ \sqrt{\frac{F_+}{F_-}}, \tag{11a}$$

$$\Sigma_e = \frac{\eta^2 \cos E}{F_+}\, \Sigma_a + \frac{e\tau}{2}\, \mathscr{B} F_- \sqrt{\frac{F_-}{F_+}} \sin^2 E, \tag{11b}$$

$$\Sigma_I = \mathscr{B} F_-^2 \sqrt{F_+ F_-} \cos^2 \zeta. \tag{11c}$$

In connection with Eqs. 10(a)–(c) resulting from changing the independent variable in the Gauss equations from time to the eccentric anomaly E, we note that for near-circular close orbits Jupp (1976) suggested an extra term (due to the drag-induced changes in a and e) to be added to the right-hand sides. Neglecting this term, the Eqs. 10(a)–(c) must be viewed only as approximate. In his answer King-Hele (1978) argued that in practice the perturbations due to odd zonal harmonics of the geopotential prevent the eccentricity to be lower than about 0.0005 (unless the inclination is zero or 65.6°), and showed that the proposed extra term is negligible except during the last day of the satellite's life, but then other simplifying assumptions of the theory are violated. The application of the TD88 theory to the near-circularly orbiting satellites discussed in this paper seems to support the idea that Jupp's term may be neglected for most of a satellite's lifetime (see especially Fig. 10, but also discussion in Section 4).

Except for the final catastrophic decay at a very low altitude, the thermospheric drag is small enough so that the orbit-averaged values of the right hand sides in Eqs. (12) are appropriate for removal of short-period perturbations and thus a good measure of the long-term effects (e.g., Milani et al., 1987). In particular,

$$Da = -a^2 \delta \int_0^{2\pi} \mathrm{d}E\, \rho \Sigma_a, \tag{12a}$$

$$De = -a \delta \int_0^{2\pi} \mathrm{d}E\, \rho \Sigma_e, \tag{12b}$$

$$DI = -a \delta\, \frac{\tau \tan I}{2\eta^2} \int_0^{2\pi} \mathrm{d}E\, \rho \Sigma_I \tag{12c}$$

are the relevant variations in one revolution.

The atmospheric perturbations of the remaining three orbital elements are generally much smaller than those from the geopotential and can be neglected for our purposes. An exception is the case of near-circular orbits, or those near the equatorial plane, for which the geopotential may cause stationary, or oscillating, values (Section 2.2.1). Since the quasi-circular orbits are of general interest, also because an evolution in an atmosphere inevitably drives orbits to that end-state, we discuss this particular case below.

In the small eccentricity limit, nonsingular elements ($k = e \cos \omega$, $h = e \sin \omega$) are the well-defined variables, indicating that $e(\mathrm{d}\omega/\mathrm{d}t)$ rather than $(\mathrm{d}\omega/\mathrm{d}t)$ is of real importance. Using the appropriate Gauss equation we have

$$e\, \frac{\mathrm{d}\omega}{\mathrm{d}E} = -a \delta \rho \Sigma_\omega, \tag{13}$$

with

$$\Sigma_\omega = \sin E \left[\frac{\eta}{F_+}\, \Sigma_a - (e + \cos E)\, \frac{e\tau}{2\eta}\, \mathscr{B} F_- \sqrt{\frac{F_-}{F_+}} \right] - \frac{e\tau}{2\eta^2} \sin I \mathscr{B} F_-^2 \sqrt{F_+ F_-} \sin \zeta \cos \zeta. \tag{14}$$

For small values of eccentricity, we may also simplify $\Sigma_\omega \simeq \sin E[1 + \mathscr{O}(e)]$. Variation in one revolution of the

satellite about the Earth is then

$$eD\omega = -a\delta \int_0^{2\pi} \mathrm{d}E \rho \Sigma_\omega. \tag{15}$$

Combining Eqs. (12b) and (15) we obtain the appropriate changes Dk and Dh of the nonsingular elements.

The cumbersome issue, necessary to evaluate the integrals in Eqs. (12) and (15), is to express the thermospheric density ρ, with its space and time variations (Section 2.1.1), in terms of the orbital elements. This topic is briefly discussed in the next paragraphs.

Thermospheric density in terms of orbital elements: We first consider the vertical-structure terms $\exp[(\bar{h}-h)/jH]$ in (3). The TD model assumes the air density is constant on the surfaces of ellipsoids of fixed flattening $\varepsilon \simeq 1/298$. To the first power in ε, the height h over the oblate Earth's surface is approximated by (e.g., King-Hele, 1964)

$$h \simeq aF_- - R(1 - \varepsilon \sin^2 \phi), \tag{16}$$

where R is the Earth's equatorial radius. Using simple spherical trigonometry we have $\sin\phi = \sin I \sin\zeta$ in terms of orbital parameters ($\zeta = \omega + f$ as before). Hence the appropriate factors in averaging are

$$c_j = \frac{\varepsilon R}{2jH} \sin^2 I, \tag{17a}$$

$$z_j = \frac{ae}{jH}, \tag{17b}$$

$$B_j = \exp\left(\frac{\bar{h}+R-a}{jH} - c_j\right), \tag{17c}$$

so that

$$\exp\left(\frac{\bar{h}-h}{jH}\right) = B_j \exp(z_j \cos E) \exp(c_j \cos 2\zeta). \tag{18}$$

While c_j are small parameters, notably the maximum value occurs for $j=1$: $c_1 \simeq 0.369 \sin^2 I$, and will be considered here of the order of eccentricity, z_j may be arbitrarily large. With this, we can expand the last exponential factor in (18) and define

$$\psi_j(\zeta) = \exp(c_j \cos 2\zeta) = 1 + c_j \cos 2\zeta + \frac{c_j^2}{2} \cos^2 2\zeta + \mathcal{O}(3). \tag{19}$$

In what follows we keep terms in c_j up to the third order included. The auxiliary angle ζ is eliminated using the transformation formulæ from the true anomaly f to the eccentric anomaly E, $\cos f = (\cos E - e)/F_-$, $\sin f = \eta \sin E/F_-$, so that ψ_j take finally the form

$$\psi_j(E) = 1 + c_j \cos 2\xi + \tfrac{1}{4} c_j^2 [1 + \cos 4\xi] + ec_j[\cos(2\xi + E) - \cos(2\xi - E)] + \cdots, \tag{20}$$

with $\xi = \omega + E$; we again keep track of terms up to the third order in c_j and e included. We finally write

$$h_n = K_n + \sum_{j=1}^{3} K_{nj} B_j \psi_j(E) \exp(z_j \cos E). \tag{21}$$

Further work also benefits from splitting the last three factors g_n in (1) into a part $\tilde{g}_n$ that changes during one revolution about the Earth and a quasi-constant part $\bar{g}_n$. We thus have $g_n = \bar{g}_n \times \tilde{g}_n$, $n = 5, 6, 7$, defined as

$$\bar{g}_5 = \sin(d - p_3), \quad \tilde{g}_5 = \sin\phi, \tag{22a}$$

$$\bar{g}_6 = 1 + a_7 f_m, \qquad \tilde{g}_6 = \sin(t - p_6)\cos\phi, \tag{22b}$$

$$\bar{g}_7 = 1 + a_8 f_m, \quad \tilde{g}_7 = \sin(2t - 2p_7)\cos^2\phi. \tag{22c}$$

Elementary spherical trigonometry yields

$$\cos t \cos\phi = -\cos I \sin\zeta \sin(\alpha - \Omega) - \cos\zeta \cos(\alpha - \Omega),$$
$$\sin t \cos\phi = -\cos I \sin\zeta \cos(\alpha - \Omega) + \cos\zeta \sin(\alpha - \Omega),$$

where α is the solar right ascension and Ω is the longitude of the ascending node. With these relations the $\tilde{g}_5 - \tilde{g}_7$ factors may be expressed in terms of the eccentric anomaly E and other orbital parameters.

The change in the semimajor axis Da over one orbital period: To show our procedure, we now focus on computing the orbit-averaged change Da from (12a). With Σ_a from (11a) we directly obtain

$$Da = -2\pi a^2 \delta f_x f_0 k_0 \times \left[\sum_{n=1}^{4} g_n \left(K_n U + \sum_{j=1}^{3} B_j K_{nj} U_j\right) + \sum_{n=5}^{7} \bar{g}_n \left(K_n V_n + \sum_{j=1}^{3} B_j K_{nj} V_{nj}\right)\right], \tag{23}$$

where the following auxiliary functions

$$U = \frac{1}{2\pi} \int_0^{2\pi} \mathrm{d}E\, \Sigma_a(E), \tag{24a}$$

$$U_j = \frac{1}{2\pi} \int_0^{2\pi} \mathrm{d}E\, \Sigma_a(E) \psi_j \exp(z_j \cos E), \tag{24b}$$

$$V_n = \frac{1}{2\pi} \int_0^{2\pi} \mathrm{d}E\, \tilde{g}_n \Sigma_a(E), \tag{24c}$$

$$V_{nj} = \frac{1}{2\pi} \int_0^{2\pi} \mathrm{d}E\, \tilde{g}_n \Sigma_a(E) \psi_j \exp(z_j \cos E) \tag{24d}$$

were introduced. Expanding the integrand in terms of small values of the eccentricity e and parameter τ in (8b), of the order of e, we obtain

$$U = (1-\tau)^2 + \tfrac{3}{4} e^2 (1 + \tau^2) + \mathcal{O}(4). \tag{25}$$

Incidentally, U and V_n can be also obtained in a closed form using the complete elliptic integrals of the first and

second kind, but without being able to obtain a similar result for U_j and V_{nj} we restrict ourselves to use the truncated series as in (25). To compute U_j we multiply ψ_j from (19) by the appropriately expanded Σ_a function; all terms are then rearranged so as to have a sum of terms each multiplied by a factor either $\sin nE$ or $\cos nE$. Thanks to the odd parity, the sine terms average out and integration of the cosine terms results in the modified Bessel functions of order n and argument z_j (see e.g., King-Hele, 1964)

$$\frac{1}{2\pi}\int_0^{2\pi}\cos(nE)\exp(z_j\cos E)\,\mathrm{d}E = I_n(z_j). \tag{26}$$

While obtaining results up to the third order in small parameters $e\sim c_j$, we give here expansion to second order only

$$\begin{aligned} U_j = {} & (1-\tau)^2 I_0(z_j) + 2e(1-\tau^2)I_1(z_j) \\ & + c_j(1-\tau)^2 I_2(z_j)\cos 2\omega \\ & + 2ec_j(1-\tau)[I_1(z_j)+I_3(z_j)]\cos 2\omega \\ & + \tfrac{3}{4}e^2(1+\tfrac{2}{3}\tau+\tau^2)[I_0(z_j)+I_2(z_j)] \\ & + \tfrac{1}{4}c_j^2(1-\tau)^2[I_0(z_j)+I_4(z_j)\cos 4\omega] + \mathcal{O}(3). \end{aligned} \tag{27}$$

Note that $I_n(z)\propto z^n$, and thus U_j can be also expressed in terms of the nonsingular elements k and h if necessary. Though straightforward, the results for V_j and V_{nj} are too lengthy and cumbersome to be reprinted here; suffice we give

$$\begin{aligned} V_5 = {} & \frac{e}{2}\Big[1+2\tau-3\tau^2 \\ & -\frac{e^2}{8}(3-2\tau+7\tau^2)+\mathcal{O}(4)\Big]\sin I\sin\omega. \end{aligned} \tag{28}$$

The overall result for Da in (23), with all necessary integrals from (24), were directly exported from Maple into computer memory in a Fortran format. The modified Bessel functions are computed using procedures from Press et al. (1992).

Other elements and comments: Integrals in (12b), (12c) and (15) are treated in the same way, with the appropriate Σ-functions from (11b), (11c) and (14). The final results are again exported as Fortran listings and used for further computations.

From all orbital elements, only the perturbation in inclination critically depends on the correct description of the thermospheric rotation (e.g., King-Hele, 1964 and Eqs. (12)). Since, on the other hand, the effects in inclination are of high interest, the issue of the thermospheric rotation merits a short comment. The zonal thermospheric winds are westward in mean, implying that $\omega_t > \omega_0$ for relevant altitudes (ω_0 is the Earth rotation speed). Despite of this consensus, less is known in detail about the order of magnitude of the effect. King-Hele and Walker (1983) review older literature and discuss new satellite observations in favour of fast zonal superrotation. Introducing Λ so that $\omega_t = \Lambda(h,\phi)\omega_0$, their results indicated $\Lambda\simeq 1.3$ at $h\simeq 300$ km and evening side of the atmosphere for low latitudes. However, the issue remains controversial, after Wharton et al. (1984) determined far smaller value $\simeq 1.04$ from Dynamics Explorer 2 in situ measurements. Theoretical studies, e.g., Mayr et al. (1984), also support slower thermospheric winds. Though a source of possible mismatch in explaining the inclination behaviour (especially for near-polar orbits), here we preliminarily neglect thermosphere's superrotation and use $\omega_t\simeq\omega_0 =$ const, and leave this issue of potential interest for further work.

2.2. Geopotential effects: zonal harmonics

To allow reasonable comparison of the satellite observations and predictions from our model, we include the principal geopotential long-term perturbations using the classical Kaula's approach (e.g., Kaula, 1962, or in more detail Kaula, 1966 or Zarrouati, 1987). With the geopotential expressed in terms of the osculating orbital elements

$$\mathscr{R}_{\ell mpq} = \frac{\kappa}{a}\left(\frac{R}{a}\right)^{\ell} F_{\ell mp}(I)G_{\ell pq}(e)S_{\ell mpq}, \tag{29}$$

where $\kappa = GM$, G is the gravitational constant, M is mass of the Earth, R the Earth reference radius, $F_{\ell mp}(I)$ and $G_{\ell pq}(e)$ the inclination and eccentricity functions, and $S_{\ell mpq}$ the appropriate trigonometric functions and geopotential coefficients, the first order analysis of the Lagrange perturbation equations yields secular terms in longitude of node ($\dot\Omega$), argument of pericentre ($\dot\omega$) and mean anomaly. Those are then used to obtain the first order effects in eccentricity and inclination, out of which we consider only the long-period parts. Hence for the eccentricity we have a contribution from the zonal harmonics of degree ℓ (we keep terms up to $\ell = 9$)

$$\Delta e_\ell = \frac{n\eta}{e\dot\omega}J_\ell\left(\frac{R}{a}\right)^{\ell}\sum_p F_{\ell 0p}G_{\ell p(2p-\ell)}\sin(\ell-2p)\omega. \tag{30}$$

Since $G_{\ell p(2p-\ell)}\propto e^{|\ell-2p|}$, the principal contribution arises when $|\ell-2p|=1$. The special case of frozen orbits ($\dot\omega=0$) near critical inclination has not been considered so far, but can be separately implemented in the future (e.g., Jupp, 1975).

Because of the axisymmetry of the zonal part of geopotential, the inclination perturbation ΔI is coupled to the eccentricity effects through

$$\Delta I = -\frac{e}{\eta^2}\frac{\cos I}{\sin I}\Delta e. \tag{31}$$

The eccentricity and inclination are thus affected primarily by the odd-degree geopotential terms (for which $\ell-2p=\pm 1$), while node and perigee by

the even-degree geopotential terms. The second-order long-period effects in e and i due to J_2 are also included (e.g., Zarrouati, 1987, p. 162).

2.2.1. Nonsingular elements for small eccentricities and/or inclinations

Kaula's analysis is not suitable for near-circular orbits, or orbits with small inclination to the reference plane, because the related angular elements (argument of perigee and longitude of node) may show markedly nonlinear, or even oscillatory, behaviour. This is because the solution of the satellite motion in the zonal geopotential field allows, in the appropriate limit, a stationary solution which is offset from circular or equatorial orbit. Since the near-circular motion is important for our work we pay particular attention to this case. A classical treatment of this problem is due to Kozai (1959) and Cook (1966); more recent is e.g., Deleflie et al. (2004a, b).

Using nonsingular orbital elements $k = e\cos\omega$ and $h = e\sin\omega$ instead of e and the ill-defined ω, the odd-degree geopotential zonals produce a small ($\sim J_2$) but nonzero systematic shift along the h-axis. Keeping the J_3 contribution only, for simplicity, we approximately have

$$k = A\cos(\sigma t + \alpha), \tag{32a}$$

$$h = A\sin(\sigma t + \alpha) + B, \tag{32b}$$

where

$$\sigma = 3nJ_2\left(\frac{R}{a}\right)^2\left(1 - \frac{5}{4}\sin^2 I\right), \tag{33a}$$

$$B = -\frac{1}{2}\frac{R}{a}\frac{J_3}{J_2}\sin I, \tag{33b}$$

A and α being constants of integration (proper values of eccentricity and argument of pericentre in the terminology of planetary studies). The parameter $B \sim J_3/J_2 \sim J_2$ is the forced eccentricity. The offset by this value along the h-axis causes nonlinear variations of perigee direction, or even its oscillations when $A < |B|$, and makes the variation in eccentricity no longer sinusoidal (see Figs. 6, 7, 10, 11). In our analysis we include effects of zonal terms up to degree nine and conventionally use description (32) in the nonsingular elements when $|B| > A/100$. Note that the osculating values of A and B may be computed from (32) by eliminating time t and from the known values of the eccentricity e and the argument of perigee ω.

Similar to the small eccentricity case, the motion with small inclination may be solved in terms of nonsingular variables ($P = \sin I\cos\Omega, Q = \sin I\sin\Omega$) which replace (I, Ω) (e.g., Kozai, 1959). We, however, do not discuss this case in detail here because in none of the examples given below these results are necessary.

2.3. Implementation of the theory

The presented TD88 theory is, therefore, semianalytic in the perturbations induced by drag and analytic in those given by the zonal terms of the geopotential. This is caused by differently treating both effects. The computation of the drag perturbations makes use of the specific formulation of the TD88 model, enabling the integration of the osculating differential equations (10) over one revolution. This basic time interval is appropriate with respect to the time scale of the changes in the thermospheric density parameters (three-hour K_p, daily values of F_x), the reinitialization performed after each integration step is desirable, because the variations in the density produced by the geomagnetic disturbances or solar flares may reach tens of percent. On the other hand, gravitational perturbations depend on the zonal coefficients J_n of the geopotential, which we take as constant in time. When adding these effects to the theory—in contrast to the perturbations given by the atmospheric drag—we could use some of the already developed methods, so we chose a well-established approach based on the classical analytical results.

The implementation of the theory in the program is basically the following. The fundamental independent variable used in our code is time. Each time step means the propagation of all necessary quantities by one solar day, $\Delta T = 86400$ s. As far as the gravitational perturbations are concerned, i.e. those due to the odd zonals in eccentricity and inclination, we just consider Eq. (30), where we take ω in the argument of trigonometric functions to advance according to $\omega = \dot{\omega}t + \omega_0$. Here time t appears explicitly. As for the atmospheric drag, Da, De, Di in Eq. (12) represent the secular changes over one anomalistic period, $P = 2\pi/n$, where n is the mean motion corrected for the perturbation given by J_2. These drag induced increments are then added to the orbital elements in the course of the propagation, each increment multiplied with a numerical factor $\Delta T/P$ reflecting the 1-day time step. So here is how we convert the "one-revolution steps" into "one-day steps" in the case of the atmospheric effects. We did not investigate the modification of the mean motion by theatmospheric drag effects, just assuming this is small for most part of the evolution. The effects of other zonal harmonics in n would be warranted for orbital arcs longer than $\simeq 200$ years.

3. Applications

We now apply the theory outlined in Section 2 to the orbits of several satellites. In doing so, certain restrictions have to be kept in mind: (i) the theory presently accounts for the drag, but not lift effects, and is best suited to spherical satellites, (ii) the orbital elements of

the example satellites in this section are propagated using the known data on solar and geomagnetic activity, what is an important condition in the lifetime prediction accuracy (see Section 3.1), and (iii) the current version of the TD model was calibrated to maximum heights of $\simeq 1200$ km so that satellites with high-altitude orbits (or those with high eccentricity) are excluded. The latter item is less constraining for satellite applications, since most of those with orbits decaying in the atmosphere within a reasonably short period of time reside at lower altitudes, but may be inconvenient for space debris applications (see Section 4). The inability to include lift effects will be addressed in the future, however a large class of laser-tracked geodynamics or other scientific satellites meet the near-sphericity requirement and their orbits are suitable for our study.

Since the theory assumes removal of short-period perturbations, a time step comparable or longer than one revolution around the Earth can be afforded. Though the shortest period in the geomagnetic effects recorded in the model is 3 h (for the K_p index), we use a time step of one day to propagate a spacecraft orbit. We verified validity of our results by using also a shorter time step, notably 3 h.

We evolve orbital elements until the semimajor axis becomes smaller than $R + 140$ km when the body is assumed burnt in the atmosphere. This empirical value has been suggested by King-Hele (1964) and it defines well the final stage of the orbital evolution of Castor (Section 3.2), GFZ-1 (Section 3.3) and other satellites.

3.1. Accuracy of lifetime prediction

We compare the prediction of the theory with the orbital data of the satellites flown in the past so that we use the measured physical parameters influencing the upper atmosphere (solar flux, index of geomagnetic activity). The uncertainty in the long-term orbit propagation then follows from atmospheric density mismodelling and uncertainty in the initial orbital data and model parameters. Since a detailed analysis of these effects is not always possible (e.g., space debris applications), uncertainties and fluctuations in some parameters are traditionally relegated to the uncertainty in the C_D coefficient.

For spherical satellites at low altitudes we assume $C_D = 2.2$ with an error of $\pm 5\%$ as discussed in Section 1. This translates into assuming C_D within the interval $\langle 2.09, 2.31\rangle$ and this directly maps onto an uncertainty interval of the computed spacecraft lifetime. We draw this "C_D-based confidence strip" in Figs. 1, 5 and 9. Quantitatively, the lifetime determination with the mean value of $C_D = 2.2$ is 0.1% (Castor), 1.8% (GFZ-1), 4.3% (Starshine 1) away from the observed value ("accuracy"), while the "confidence interval" defined by the limiting values of C_D represents $\pm 2.2\%$ (Castor), $\pm 2.6\%$ (GFZ-1), $\pm 5.5\%$ (Starshine 1) relative to the mean lifetime prediction ("precision"). In each of the examples below we also determined the best suited value of $C_D$for which the theory yields the observed lifetime value, which are 2.18 (Castor), 2.12 (GFZ-1) and 2.10 (Starshine 1). For Starlette and Grid Sphere satellites (Figs. 12 and 13), residing in the altitude range 800–1200 km, we modified the "C_D-based confidence strip" to encompass the variation of the drag coefficient in these heights, $C_D \in \langle 2.1, 3\rangle$ (Zarrouati, 1987).

Note on the accuracy of lifetime prediction for future missions: The accuracy of the lifetime prediction for low Earth satellites is limited by two contributions at least: (i) the incompleteness or uncertainty in the force model (such as discussed above), and (ii) the uncertainty in modelling the future behaviour of solar activity necessary for the atmospheric drag effects. The latter issue is usually more serious. Modelling the 11-year variability of solar activity is complicated not only by the significant irregularities in the average profile of each cycle (this can be modelled e.g., by taking minimum and maximum peak profiles), but especially because of the unequal length of a particular cycle. Differences in the length of cycles may be as large as 11%, producing up to a year uncertainty in the prediction of the moment when a particular cycle will start. This has a vast influence on the lifetime prediction (see Owens et al., 2000).

To have an order-of-magnitude idea illustrating these effects, we consider the case of spacecraft Castor (Section 3.2). The lifetime prediction with our theory and with extrapolated solar activity becomes inaccurate by $\pm 27\%$; this compares with about $\pm 2.2\%$ inaccuracy when solar activity is known.

3.2. Castor (1975-039B)

The French microsatellite Castor has played a prominent role in the history of in situ measurements of the thermospheric density: carrying an accurate microaccelerometer it was an early mission that allowed long-term and coherent series of measurements of nongravitational perturbations on a low-flying satellite (Boudon et al., 1979; Falin et al., 1981). Castor had a nearly spherical shape with a diameter $d \simeq 75.6$ cm and a mass of $m = 77.5$ kg. The initial orbit, with inclination $\simeq 30^\circ$, had a perigee at $\simeq 270$ km and apogee at $\simeq 1270$ km. Launched on 17 May, 1975, the satellite acquired data mainly during the solar minimum phase and decayed in the atmosphere after $\simeq 1373$ days. Thanks to a collaboration with OCA/CERGA at Grasse, we had the opportunity to obtain Castor measurements, including a rather detailed information about its orbital evolution. This is used to compare with the theory in Section 2.

Figs. 1–4 show that comparison during the whole lifetime. Observations are represented by the averaged

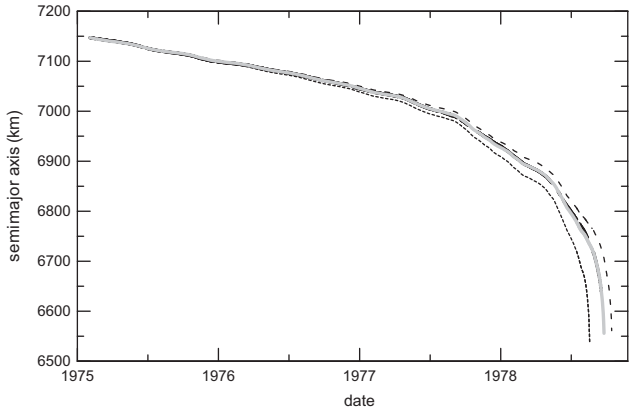

Fig. 1. Long-term decrease of Castor's semimajor axis during its lifetime. Dots are measurements, solid line is the TD88 model with $C_D = 2.18$ (for most part their difference is too small to be noticed; typical fractional difference of the computed solution and observartions is $\simeq \pm 0.02\%$). Solutions with $\pm 5\%$ variation of the C_D coefficient from a nominal value of 2.2, defining the C_D-based confidence strip discussed in the text, are also shown: (i) $C_D = 2.09$ (long-dashed line), and (ii) $C_D = 2.31$ (short-dashed line).

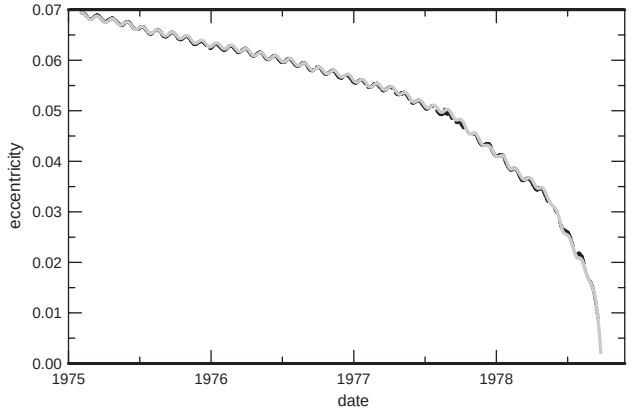

Fig. 2. As in Fig. 1 but for Castor's eccentricity (and the $C_D = 2.18$ value; variations of C_D are not shown here). The secular trend is due to the atmospheric drag, long-periodic variations due to the odd zonal harmonics of the geopotential (principally the J_3 term).

osculating elements with a running window of a day length; although the data are nonuniform, we suppose this approximative method of removing the short-period perturbations to be satisfactory here, as the gaps in the data are generally of small size and placed irregularly. The computed orbit assumed a single set of initial data and adjusted C_D coefficient to achieve the best possible value of lifetime. Obviously, C_D is fully correlated with the S/m ratio (Eq. (8a)), whose average variations (standard error) reach $\simeq 3\%$. This effect, together with compositional variations at different heights and surface characteristics of the satellite, may contribute to the effective variations of C_D, as well as the average density errors in the density model. Nevertheless, we see in Fig. 1 that the nominal value (2.2) is very close to the lifetime best fitting value of 2.18. We warn the reader that such a perfect agreement in the orbital lifetime may be accidental in part, and itis not likely to be the case of

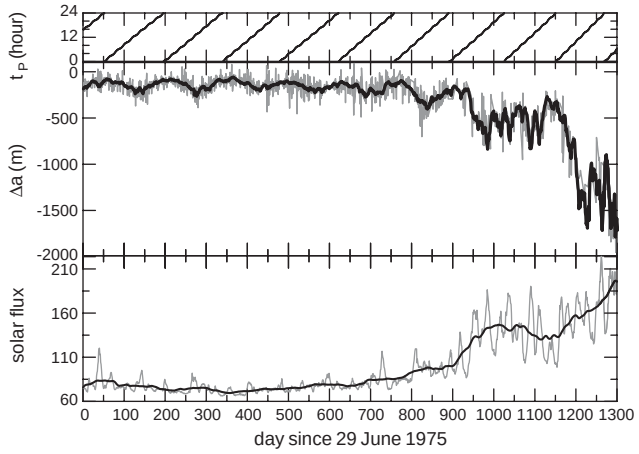

Fig. 3. Middle panel: Castor's semimajor axis variations—ordinate shows the daily change Δa due to atmospheric drag. Observations (grey solid line) are shown together with model results (black solid line). During the low solar activity phase, time $\leqslant 800$ days, the principal long-term variation is due to circulation of the satellite perigee as referred to the Sun—perigee hour angle t_P—shown in the upper panel. As the solar activity increases, determined by the daily values F_x (grey solid line) and the three-month average value F_b (black solid line) of the solar 10.7-cm flux shown in the bottom panel, semimajor axis variations become larger and erratic. The model, however, still appears to explain its principal variations. A correlation between the sudden peaks of the solar activity and large excursions in the semimajor axis perturbations due to the atmospheric density variations are easily seen. The net decrease of the semimajor axis at the end is a combination of two effects: (i) the overall increase of the solar activity diagnosed by the F_b parameter, and (ii) systematically smaller perigee height.

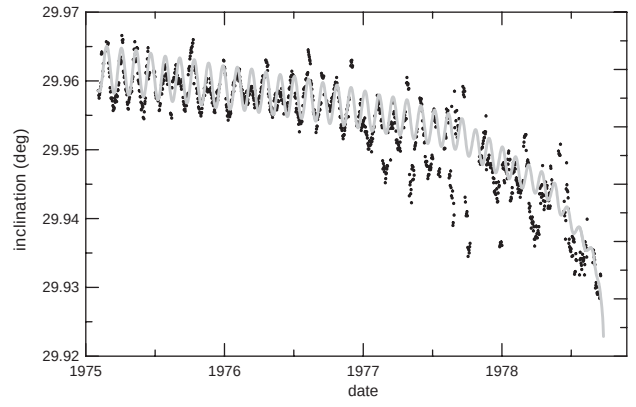

Fig. 4. As in Fig. 2 but for Castor's inclination. Long-periodic effects are due to the odd zonal harmonics of the geopotential (principally the J_3 term), while the $\simeq 0.04^\circ$ decrease at the end of the mission is due to the drag in the corotating atmosphere. The inclination is observationally determined with the least accuracy, though some mismatch in the signal is caused by the lack of modelled lunisolar perturbations.

other satellites. However, we anyway consider the agreement of the theory and observations rather satisfactory, especially for the semimajor axis and the eccentricity. For instance the fractional difference of the computed and observed values of the semimajor axis does not exceed 0.02% for most the lifetime and does not indicate any linear drift; larger difference occurs only during the final decrease in the atmosphere.

Another approach to see high sensitivity of the orbital decay on the environmental effects is in Fig. 3, which shows the daily changes in Castor's semimajor axis. First, during the low solar activity period the secular drag is small and the prevailing long-period effect is an oscillation with a period of $\simeq 143$ days due to changing mutual geometry of the satellite elliptic orbit and the solar direction (the corresponding terms involving longitude of perigee ϖ and the solar right ascension α were readily identified); this is what Jacchia (1959a, b) calls the "diurnal effect" and corresponds to the orbit plane passing through the bulge in the atmosphere, while the periapsis being on the dayside. When solar activity increases, variations of semimajor axis become much more erratic and mainly reflect principal solar flares and geomagnetic state. The fact that the thermospheric density fluctuates with these solar disturbances has been previously reported many times, in particular from the density measurements of Castor itself (e.g., Villain et al., 1979; Falin et al., 1981; Berger and Barlier, 1981). The net effect is then given by the overall solar activity level, characterized here by the three-month average F_b of the solar radio flux; obviously, decrease of the meanaltitude above the Earth toward the end of the mission also contributes to larger daily changes Δa.

Fig. 4 shows long-term variation of Castor's inclination. A large jitter in the observations is mainly due to observational inaccuracy. We roughly tested the hypothesis of atmospheric superrotation with a simple assumption of a constant value of the Λ parameter. Apparently, all solutions with $\Lambda \in (1, 1.15)$ match the observations, while only those with $\Lambda > 1.25$ fail to fit them. Inaccuracy in the data, however, did not allow us to draw any specific conclusions about mean value of atmospheric superrotation from Castor's data.

3.3. GFZ-1 (1995-020A)

In this case our knowledge about the satellite and its orbital parameters was not so detailed as in the Castor's case; we used data from http://op.gfz-potsdam.de/gfz1/gfz1.html. GFZ-1 was designed as a small, passive, spherical satellite ($d = 21.5$ cm, $m = 20.63$ kg), equipped with retro-reflectors to be tracked from the ground by the satellite laser ranging systems. The satellite was released from MIR on 19 April 1995 into a nearly spherical orbit at an altitude of 390 km with the inclination of 51.6°, and decayed after $\simeq 1525$ days.

The orbital data and model predictions are compared in Figs. 5–8. Data were obtained from the two-line element series with the short-term gravitational perturbations removed using a modified SGP4 procedure with J_2-induced short perturbations removed (for the definition standard SGP4 procedure, see Hoots and Roehrich, 1980). The GFZ-1 orbit is interesting for testing our predictions because of its very small eccentricity, $e \simeq 0.0008$ on average; thus description in nonsingular elements is used throughout the, entire lifetime. We again observe admittedly good agreement between the theoretical and observed values, with the best fit of the satellite lifetime for $C_D = 2.12$. This value is within the $\pm 5\%$ tolerance around the nominal value of 2.2 and is in reasonable agreement with SLR-derived results giving the average C_D of 2.05 (Cox and Lemoine, 1999). The simulated lifetime for $C_D = 2.2$ is 31 days (i.e. 2% of the lifetime) away from the observed value.

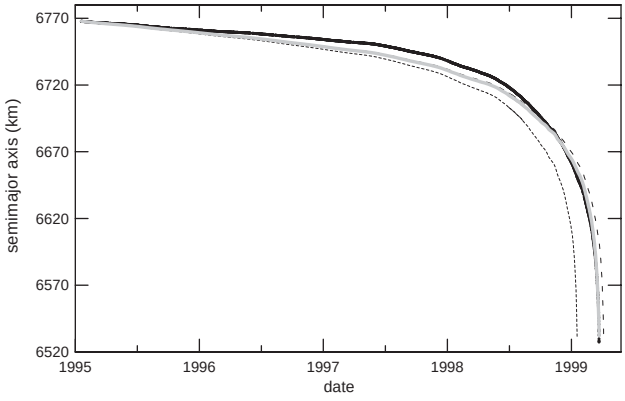

Fig. 5. Long-term decrease of the semimajor axis for GFZ-1 satellite during its lifetime of $\simeq 1525$ days. The best fit to the orbital lifetime is provided by assuming $C_D = 2.12$ (solid line); data (black dots). The effect of $\pm 5\%$ variations in C_D around the nominal value of 2.2 is shown by the dashed lines: (i) $C_D = 2.09$ long-dashed line, and (ii) $C_D = 2.31$ short-dashed line.

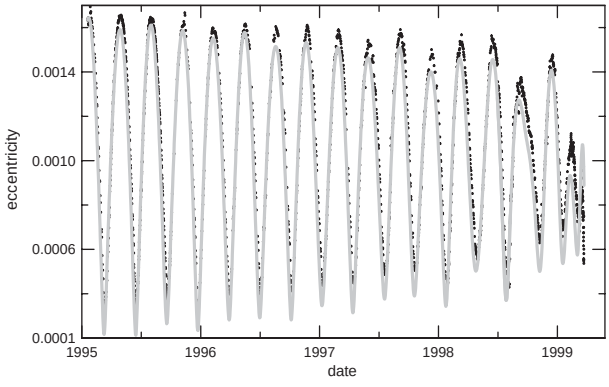

Fig. 6. As in Fig. 5 but for GFZ-1's eccentricity. Observations (dots) are well-matched by the model (solid line): the initial steady oscillations are due to the zonal harmonic terms in geopotential, while the atmospheric drag contributes to the late behaviour.

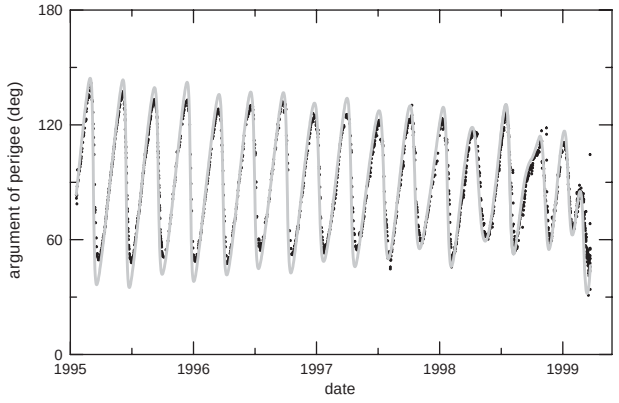

Fig. 7. As in Fig. 5 but for GFZ-1's argument of perigee ω. Due to the low eccentricity (Fig. 6), ω liberates around 90° value, rather than circulates. Atmospheric drag causes the stable point of the gravitational perturbation to migrate towards the smaller value and, in the same time, diminishes its variations; both effects are seen during the late phase of evolution. Observations (dots) are again compared with the theoretical curve (solid line).

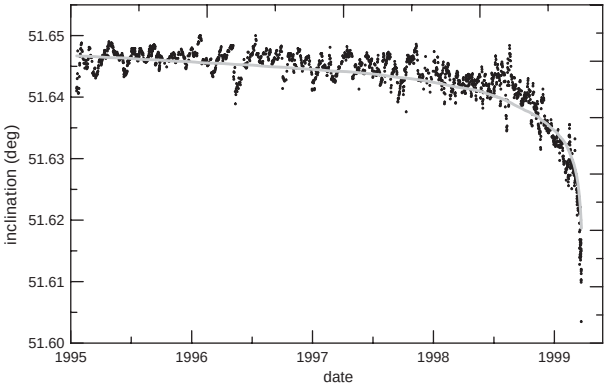

Fig. 8. As in Fig. 5 but for GFZ-1's inclination. The overall decrease in the observations (dots) as modelled by our drag theory (solid line); the long-term oscillations are caused mainly by the lunisolar perturbations.

Both eccentricity and argument of perigee, Figs. 6 and 7, are also well fitted with the combined effect of the odd zonal terms in geopotential and the atmospheric drag. The latter tends to circularize the orbits proper value and, an the same time, also displaces the fixed point of the argument of perigee due to the gravitational effects (at 90°, Section 2.2.1) to a smaller value.

3.4. Starshine 1 (1999-030B)

Orbital data for this satellite have been obtained from NASA/GSFC Orbital Information Group Web Site (http://oig1.gsfc.nasa.gov/) as two-line element series. Starshine 1 was the first of three small, optically reflective spherical student satellites that have been designed by the US Naval Research Laboratory and built by a volunteer coalition of organizations and individuals in the USA and Canada. Starshine 1 was deployed on 5 June 1999 into a nearly circular orbit with an initial altitude of 388 km and inclination of 51.6°. The satellite reentered the atmosphere after a 258 day flight, on 18 February 2000. Physical parameters, notably size of $d = 48.3$ cm and mass $m = 39.3$ kg, are from http://azinet.com/starshine/. Moore et al. (2003) presented a preliminary analysis of Starshine orbital data for an independent test of Naval Research Laboratory upper atmosphere density models.

To compare Starshine's orbital evolution with our model prediction (Figs. 9–11) we again removed short-term gravitational perturbations from the two-line elements using the SGP4 model (Hoots and Roehrich, 1980). The best fit value of C_D coefficient is 2.10, smaller

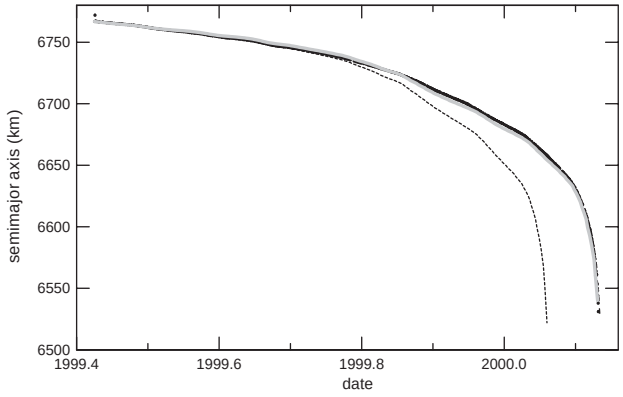

Fig. 9. Long-term decrease of Starshine's semimajor axis during its lifetime. The best fit to the observed lifetime is provided by assuming $C_D = 2.10$ (solid line); data (black dots). The effect of ±5% variations in C_D around the nominal value of 2.2 is shown by the dashed lines: (i) $C_D = 2.09$ long-dashed line, and (ii) $C_D = 2.31$ short-dashed line.

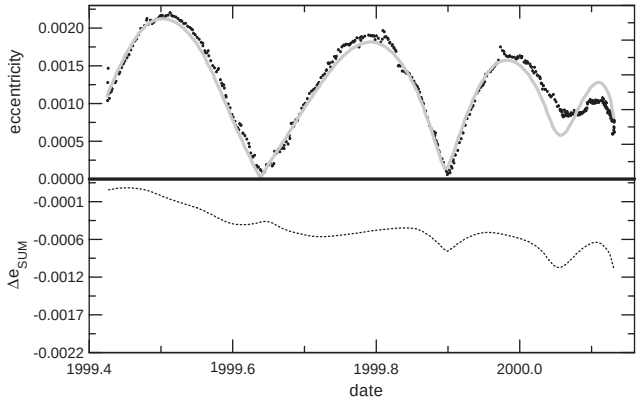

Fig. 10. As in Fig. 5 but for Starshine's eccentricity. Top: observations (symbols) compared with the model prediction (solid line). Bottom: the accumulated eccentricity change due to the atmospheric drag only. Atmospheric drag causes the stable point of the gravitational perturbation to migrate towards the smaller value of eccentricity and, in the same time, diminishes its variations.

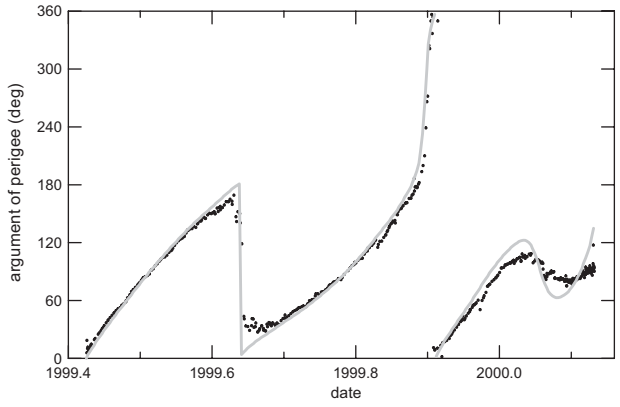

Fig. 11. As in Fig. 5 but for Starshine's argument of perigee. The amplitude of circulation about the equilibrium (forced) eccentricity is initially comparable to its offset from the origin in the nonsingular elements (h, k) making thus the apparent discontinuities in September and November 1999. Later the atmospheric drag damps the amplitude to cause more regular oscillations around the 90° equilibrium value.

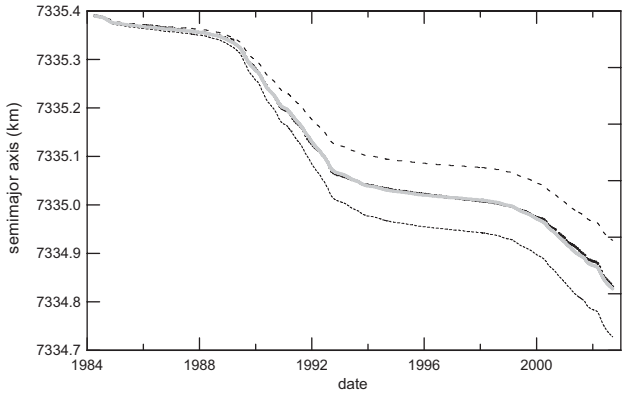

Fig. 12. Long-term decrease of Starlette's semimajor axis over an 18-year period. Steeper variation in between 1987 and mid 1992, and after 1999, correlates with periods of high solar activity. Symbols are the observed orbit, the solid line is the best fit with the TD model, assuming $C_D = 2.55$ for the drag coefficient. The two dashed lines show solutions with $C_D = 2.1$ (short-dashed) and $C_D = 3$ (long-dashed), physically motivated limiting values of this parameter.

than its nominal value of 2.2. In spite of similar initial data as in the GFZ-1 case, Starshine 1 reentered much faster; this is because maximum of solar activity occurring in 2000. The small eccentricity of Starshine makes the evolution of argument of pericentre highly nonlinear (Fig. 11); one can notice two interesting cases, in July 1999 and in November 1999, when the orbit becomes nearly circular with ω quickly travelling close to the zero degree value. Yet, our model seems to explain this effect rather well.

3.5. Starlette (1975-010A) and Grid Sphere 7-1 (1971-067E)

Starlette, launched on 6 February, 1975 by the French space agency CNES, was a first in a series of successful laser-tracked geodynamics satellites. Small and dense, with a diameter of $\simeq 21$ cm and mass of $\simeq 47.3$ kg, its primary goal is to probe the Earth's gravitational field. The initial perigee altitude of $\simeq 810$ km, high orbit determination accuracy requirements and long time span of observations require that atmospheric drag must be taken into account in a precise orbit determination. As an example, Bruinsma et al. (1999) used the Starlette orbital data to assess the accuracy of several thermospheric density models. As a part of their analysis, they also obtained long-term variations of the observed orbital elements by accurate filtering techniques, and these have been kindly provided to us.

The first obstacle in our work, however, was to extend the original TD model to higher altitudes, appropriate for the Starlette orbit. Using a similar technique as in Sehnal and Pospíšilová (1988) we adjusted the TD model parameters to achieve the best possible agreement between TD density predictions and those from DTM94 model (Berger et al., 1998). The tested height range was 750–1200 km, the parameter set is given in Appendix B. With the new model we were able to propagate Starlette's orbit using the theory in Section 2 and compare it with observations. Fig. 12 shows this comparison for semimajor axis during an 18-year period. The best fit is obtained with $C_D \simeq 2.55$, significantly larger than for the low-altitude satellites discussed above. This finding is in a good agreement with theory that expects a strong altitude dependence of C_D in between 500 and 1000 km. As an example, models discussed in Zarrouati (1987) determine for Starlette's altitude C_D in the 2.1–3 range, depending on the value ofexospheric temperature T_∞. Our best fit value of 2.55 incidentally corresponds to its theoretical value at 800 km and T_∞ for mean atmospheric conditions. The timescale shown in Fig. 12 allows to appreciate the difference in the net semimajor-axis decay-rate for periods of solar minimum and maximum activity, respectively.

Another example of a spacecraft flying above the nominal height range of the former TD88 model is Grid Sphere 7-1, launched on 7 August 1971 onto a near polar ($I \simeq 87.6°$) and near circular ($e \simeq 0.01$) orbit with initial perigee height of $\simeq 790$ km. Grid Sphere was part of a fleet of experimental atmospheric satellites all ejected from the same booster OV1-21. In this case, the satellite was a rigid aluminium sphere that served as a radar calibration target. The satellite has a markedly large value of the area-to-mass ratio: $d = 1.12$ m for $m = 37$ kg. Two-line elements, obtained from http://

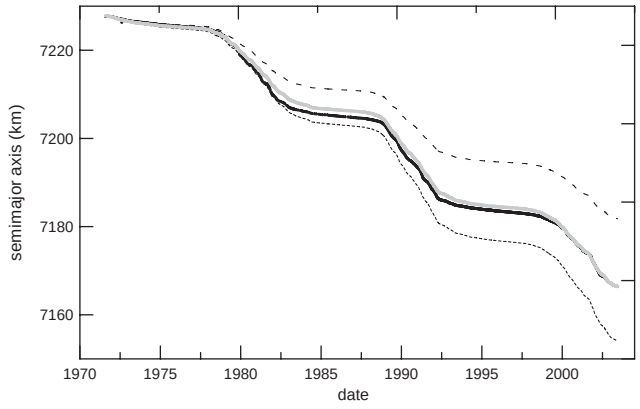

Fig. 13. Long-term decrease of Grid Sphere's semimajor axis over a 32-year period. As in the case of Starlette, Fig. 12, steeper variations indicate periods of maximum solar activity. Symbols are the observed orbit, the solid line is the best fit with the TD model, assuming an initial value of the drag coefficient $C_D = 2.63$. The two dashed lines show solutions with $C_D = 2.1$ (short-dashed) and $C_D = 3$ (long-dashed), physically motivated limiting values of this parameter.

oig1.gsfc.nasa.gov/, were handled as in the case of GFZ-1 and Starshine 1 above.

Fig. 13 shows the long-term behaviour of Grid Sphere's semimajor axis obtained by the propagation with our model and with the modified density parameters from Appendix B. A fairly good agreement is obtained with $C_D = 2.63$, a value similar to that of Starlette. The sequence of shallower and steeper variations of Grid Sphere's semimajor axis reflect solar cycles; their unequal length can be easily noticed.

4. Conclusions

The purpose of this work is to investigate long-term orbital dynamics of low-altitude satellites or debris particles using a semianalytic theory of motion. The goal is to develop a fast computational tool enabling to propagate vast amounts of real or fictitious orbits which may be useful for studying multiparameter orbital problems or evolution of a space debris population (e.g., Walker et al., 1997; Rossi et al., 1998; Reynolds et al., 1999). In order to validate the theory, we compared its predictions with the orbital data of several artificial satellites. In spite of the limitations and constraints due to model assumptions and its incompleteness, we may conclude their reasonably fair agreement. In particular, the estimated lifetime differs from the observed value by a few percent typically. This, however, becomes about an order of magnitude worse for extrapolation to the future because of the limitations in the prediction of solar activity.

Despite the fair agreement between the theory and observations discussed above, the theory would profit from further improvements. First, the TD model itself should be reanalysed with the goal of obtaining a better agreement with predictions of newer versions of aeronomic models such as NRLMSIS or DTM2000. Second, further effects, such as those mentioned at the beginning of Section 2, might be straightforwardly included in the theory. Finally, the theory of orbital motion in a resistive medium should be further investigated to allow its broader applicability. As an example, in Section 2.1.2 we noted that the classical averaging in the eccentric anomaly, inherited from classical works of King-Hele and others, may be invalid for low eccentricities (also Jupp, 1976). In the case of macroscopic artificial satellites, the caveat is insignificant since the geopotential perturbations typically force eccentricity above the critical value below which simple, King-Hele-type averaging is unjustified. However, since $\delta \propto S/m \propto 1/r$, with r being linear dimension of the body, this critical eccentricity may become $\geqslant 0.01$–0.1 for millimetre to centimetre sized debris particles. Another example is inability to treat high-eccentric orbits which may be important for space debris applications. An impulsive approximation, similar to that in Hoots and France (1987)should be investigated.

Note. The online calculation as well as the Fortran 77 code are available through the web site http://www.asu.cas.cz/~bezdek/density_therm/pohtd/.

Acknowledgements

We thank C. Berger and F. Barlier for providing us with detailed information, including microaccelerometric measurements and orbital data, about the Castor mission (Section 3.2). P. Exertier kindly provided the filtered orbital elements of Starlette satellite (Section 3.5). We also thank both referees for their useful comments.

Appendix A. Parameters of the TD model

Sehnal and Pospíšilová (1988) derived the following numerical parameters of the TD model appropriate for the height range of 150–750 km: (i) the scale height $H = 29$ km, (ii) the parameters a_n, with $n = 1 \ldots 8$, and (iii) the phases p_n, with $n = 3 \ldots 7, >$

$$a_n = [.007, .2875, .04762, .0471, 7, 7, .3333, 15],$$
$$p_n = [-29.41, -263, 263, 8.0913, 10.0813],$$

(iv) the constants K_{nj}, with $n = 1 \ldots 7$ and $j = 1 \ldots 3$,

$$K_{nj} = \begin{bmatrix} .766373(-8) & .16573(-9) & .3871(-10) \\ -.440149(-8) & .33428(-9) & .9352(-10) \\ .118107(-9) & -.14781(-9) & -.1518(-11) \\ -.159664(-10) & -.64670(-11) & -.2050(-11) \\ -.240755(-9) & -.13985(-10) & -.3059(-11) \\ .643785(-10) & .13618(-9) & .3517(-10) \\ .744666(-11) & .45416(-11) & .2080(-11) \end{bmatrix}, \tag{A.1}$$

and (v) the constants K_n, with $n = 1 \ldots 7$

$$K_n = [.296815(-14), .281456(-13), -.123300(-13), \\ -.114892(-16), -.390065(-15), .742439(-14), \\ -.341594(-15)].$$

These are considered to be nominal values and used for all satellite orbits, except for Starlette and Grid Sphere in Section 3.5.

Appendix B. Extension of the TD model to higher altitudes

To enable higher orbits, we used the following modified numerical parameters of the TD model suitable for altitudes in the 750–1200 km range: (i) the scale height $H = 27.85229$ km, (ii) the parameters a_n

$$a_n = [0.007243, 0.1778, 0.1449, -0.01179, 7.011, 6.968, \\ 3.301, 14.91],$$

(iii) the constants K_{nj} read

$$K_{nj} = \begin{bmatrix} .766348(-8) & .15645(-9) & .1943(-10) \\ -.440146(-8) & .36649(-9) & .2661(-9) \\ .118107(-9) & -.14007(-9) & -.1470(-11) \\ -.159664(-10) & -.65029(-11) & -.2317(-11) \\ -.240756(-9) & -.14318(-10) & -.3506(-11) \\ .643785(-10) & .14922(-9) & .2019(-10) \\ .744666(-11) & .44938(-11) & .2066(-11) \end{bmatrix}, \tag{B.1}$$

and (iv) the constants K_n, with $n = 1 \ldots 7$

$$K_n = [.352814(-14), .807687(-14), .845184(-15), \\ -.116620(-16), -.260648(-15), .991392(-15), \\ .699853(-16)].$$

The phases p_n were same as in Appendix A. These values follow from a nonlinear fit of the 686 thousand TD model density predictions compared with the DTM94 model values (Berger et al., 1998); isotropic spatial distribution of the tested locations and uniform distribution of heights (in the required range), solar and geomagnetic activity parameters was used.

References

Barlier, F., Berger, C., 1983. A point of view on semi-empirical thermospheric models. Planet. Space Sci. 31 (9), 945–966.

Barlier, F., Berger, C., Falin, J.L., Kockarts, G., Thuillier, G., 1978. Ann. Geophys. 34, 9–24.

Berger, C., Barlier, F., 1981. Asymmetrical structure in the thermosphere during magnetic storms as deduced from the CACTUS accelerometer data. Adv. Space Res. 1, 231–235.

Berger, C., Biancale, R., Ill, M., Barlier, F., 1998. Improvement of the empirical thermospheric model DTM: DTM94—a comparative review of various temporal variations and prospects in space geodesy applications. J. Geodesy 72, 161–178.

Boudon, Y., Barlier, F., Bernard, A., Juillerat, R., Mainguy, A.M., Walch, J.J., 1979. Synthesis of flight results of the Cactus accelerometer for accelerations below 10^{-9} g. Acta Astronaut. 6, 1387–1398.

Breiter, S., Métris, G., 1999. Symplectic mapping for satellites and space debris including nongravitational forces. Celest. Mech. Dyn. Astron. 71, 79–94.

Brouwer, D., 1963. Review of celestial mechanics. Ann. Rev. Astron. Astrophys. 1, 219–234.

Brouwer, D., Hori, G., 1961. Theoretical evaluation of atmospheric drag effects in the motion of an artificial satellite. Astron. J. 66, 193–225.

Bruinsma, S.L., Exertier, P., Biancale, R., 1999. An assessment of new satellite total density data for improving upper atmosphere models. Planet. Space Sci. 47, 1465–1473.

Casotto, S., 1991. Spectral decomposition of geopotential. Earth and ocean tidal perturbations in linear satellite theory. Celest. Mech. Dyn. Astron. 50, 125–141.

Cook, G.E., 1966. Perturbations of near-circular orbits by the Earth's gravitational potential. Planet. Space Sci. 14, 433–444.

Cox, C.M., Lemoine, F.G., 1999. Precise orbit determination of the low altitude spacecraft, TRMM, GFZ-1, and EP/EUVE using improved drag models. AAS 99-189. Adv. Astronaut. Sci. 102, 1277.

Danielson, D.A., Sagovac, C.P., Neta, B., Early, L.W., 1995. Semianalytic satellite theory (SST): mathematical algorithms. NPS-MA-95-002, Technical Report Naval Postgraduate School, Monterey, CA.

de Lafontaine, J., Hughes, P., 1983. An analytic version of Jacchia's 1977 model atmosphere. Celestial Mech. 29, 3–26.

Delhaise, F., 1991. Analytical treatment of air drag and Earth oblateness effects upon an artificial satellite. Cel. Mech. Dyn. Astron. 52, 85–103.

Deleflie, F., Métris, G., Exertier, P., 2004a. Circular orbits: how defining a variation of the perigee really secular. Celest. Mech. Dyn. Astron., in press.

Deleflie, F., Métris, G., Exertier, P., 2004b. An analytical solution of the Lagrange planetary equations valid also from very low eccentricities. Celest. Mech. Dyn. Astron., submitted for publication.

Falin, J.-L., Kockarts, G., Barlier, F., 1981. Densities from the CACTUS accelerometer as an external test of the validity of the thermospheric models. Adv. Space Res. 1 (12), 221–225.

Fitzpatrick, P.M., 1970. Principles of Celestial Mechanics. Academic Press, New York.

Fonte, D.J., Neta, B., Sabol, C., Danielson, D.A., Dyar, W.R., 1995. Comparison of Orbit Propagators in the Research and Development Goddard Trajectory Determination System (R&D GTDS). Part I: Simulated Data. AAS 95-431, Proceedings of AAS/AIAA

Astrodynamics Specialist Conference, Halifax, Nova Scotia, August 14–17.
Giacaglia, G.E.O., 1973. Lunar perturbations on artificial satellites of the Earth. SAO Special Report, 352.
Gill, E., 1996. Smooth Bi-polynomial Interpolation of Jacchia 1971 Atmospheric Densities For Efficient Satellite Drag Computation. DLR-GSOC IB 96-1.
Gooding, R.H., 1981. On the generation of satellite position /and velocity/ by a mixed analytical-numerical procedure. Adv. Space Res. 1 (6), 83–93.
Hedin, A.E., 1983. A revised thermospheric model based on mass spectrometer and incoherent scatter data: MSIS-83. J. Geophys. Res. 88, 10,170.
Hedin, A.E., 1987. MSIS-86 thermospheric model. J. Geophys. Res. 92, 4649.
Hedin, A.E., 1991. Extension of the MSIS thermosphere model into the middle and lower atmosphere. J. Geophys. Res. 96, 1159.
Helali, Y.E., 1987. Perturbations in the perigee distance due to atmospheric drag for artificial Earth satellites. Bull. Astron. Inst. Czech. 38, 329–334.
Hoots, F.R., France, R.G., 1987. An analytic satellite theory using gravity and a dynamic atmosphere. Celestial Mech. 40, 1–18.
Hoots, F.R., France, R.G., 1997. The future of artificial satellite theories. Celestial Mech. 66, 51–60.
Hoots, F.R., Roehrich, R.L., 1980. Models for propagation of NORAD element sets. Project Spacecraft Report No. 3, Aerospace Defense Command, United States Air Force; package compiled by T.S. Kelso, 1988, http://celestrak.com/.
Jacchia, L.G., 1959a. Two atmospheric effects in the orbital acceleration of artificial satellites. Nature 183, 526–527.
Jacchia, L. G., 1959b. Solar effects on the acceleration of artificial satellites. SAO Special Report 29.
Jacchia, L.G., 1960. A variable atmospheric-density model from satellite accelerations. SAO Special Report 39.
Jacchia, L.G., 1961. The atmospheric drag of artificial satellites during the October 1960 and November 1960 events. SAO Special Report 62.
Jacchia, L.G., 1964. Static diffusion models of the upper atmosphere with empirical temperature profiles. SAO Special Report 170.
Jacchia, L.G., 1970. New static models of the thermosphere and exosphere with empirical temperature profiles. SAO Special Report 313.
Jacchia, L.G., 1971. Revised static models of the thermosphere and exosphere with empirical temperature profiles. SAO Special Report 332.
Jacchia, L.G., 1977. Thermospheric temperature, density, and composition: new models. SAO Special Report 375.
Jacchia, L.G., Slowey, J., 1962a. Preliminary analysis of the atmospheric drag of the twelve-foot balloon satellite (1961 δ1). SAO Special Report 84.
Jacchia, L.G., Slowey, J., 1962b. Accurate drag determinations for eight artificial satellites: atmospheric densities and temperatures. SAO Special Report 100.
Jupp, A.H., 1975. The problem of the criticial inclination revisited. Celestial Mech. 11, 361–378.
Jupp, A.H., 1976. Some investigations into the atmospheric drag problem. Celestial Mech. 14, 335–339.
Kaula, W.M., 1962. Development of the lunar and solar disturbing functions for a close satellite. Astron. J. 67, 300–303.
Kaula, W.M., 1966. Theory of Satellite Geodesy. Blaisdell, Waltham MA.
King-Hele, D., 1964. Theory of Satellite Orbits in an Atmosphere. Butterworth, London.
King-Hele, D., 1978. Comment on the Paper 'Some investigations into the atmospheric drag problem' by A.H. Jupp. Celestial Mech. 18, 163–164.
King-Hele, D.G., Walker, D.M.C., 1959. Irregularities in the density of the upper atmosphere: results from satellites. Nature 183, 527–529.
King-Hele, D., Walker, D.M.C., 1983. Upper-atmosphere zonal winds from satellite orbit analysis. Planet. Space Sci. 31, 509–535.
Kozai, Y., 1959. The motion of a close earth satellite. Astron. J. 64, 367–377.
Kozai, Y., 1973. A new method to compute lunisolar perturbations in satellite motions. SAO Special Report 349.
Laplace, P.S., 1805. Traité de Mécanique Céleste, Tom IV, Par 2. Courcier, Paris.
Lathuillère, C., Menvielle, M., Lilensten, J., Amari, T., Radicella, S.M., 2002. From the Sun's atmosphere to the Earth's atmosphere: an overview of scientific models available for space weather developments. Ann. Geophys. 20, 1,081–1,104.
Marcos, F.A., 2002. AFRL Satellite Drag Research. The 2002 Core Technologies for Space Systems Conference, Colorado Springs, Colorado, November 19–21, http://www.spacecoretech.org/coretech2002/.
Mayr, H.G., Harris, I., Hedin, A.E., Spencer, N.W., Wharton, L.E., 1984. Thermospheric superrotation revisited. J. Geophys. Res. 89, 5,613–5,624.
Milani, A., Nobili, A.M., Farinella, P., 1987. Nongravitational Perturbations and Satellite Geodesy. A. Hilger, Bristol.
Moe, M.M., Wallace, S.D., Moe, K., 1993. Refinements in determining satellite drag coefficients: method for resolving density discrepancies. J. Guidance Control Dyn. 16, 441–445.
Moe, K., Moe, M.M., Wallace, S.D., 1996. Drag coefficients of spheres in free-molecular flow, AAS 96-126. Adv. Astronaut. Sci. 93, 391–405.
Moe, K., Moe, M.M., Wallace, S.D., 1998. Improved satellite drag coefficient calculations from orbital measurements of energy accommodation. J. Spacecraft Rockets 35 (3), 266–272.
Montenbruck, O., Gill, E., 2001. Satellite Orbits. Springer, Berlin.
Moore, R.G., et al., 2003. Upper atmospheric densities derived from Starshine spacecraft orbits, presented at 17th Annual AIAA Conference on Small Satellites, Utah.
Musen, P., 1961. On the long-period lunar and solar effects on the motion of an artificial satellite. J. Geophys. Res. 66, 2,797–2,805.
Newton, I., 1687. Philosophiae Naturalis Principia Mathematica. Book II, Section IV, London; English translation by F. Cajori, Newton's Principia, University of California Press, Berkeley, 1934.
Owens, J.K., Vaughan, W.W., Niehuss, K.O., Minow, J., 2000. Space weather, earth's neutral upper atmosphere (thermosphere), and spacecraft orbital lifetime/dynamics. IEEE Trans. Plasma Sci. 28(6), http://www.eng.auburn.edu/users/kirkih/UZB411E-lectures/HW-3_Reading.pdf, pp. 1920–1930.
Picone, J.M., Hedin, A.E., Drob, D.P., Aikin, A.C., 2002. NRLMSISE-00 empirical model of the atmosphere: statistical comparisons and scientific issues. J. Geophys. Res. 107 (A12), 1468.
Press, W.H., Teukolsky, S.A., Vetterling, W.T., Flannery, B.P., 1992. Numerical recipes in Fortran. Cambridge University Press, Cambridge.
Reynolds, R., Eichler, P., Bade, A., Krisko, P., Johnson, N., 1999. Sensitivity analysis of the orbital debris environment using the EVOLVE 4.0 model. Adv. Space Res. 23 (1), 175–185.
Rossi, A., Anselmo, L., Cordelli, A., Farinella, P., Pardini, C., 1998. Modelling the evolution of the space debris population. Planet. Space Sci. 46, 1583–1596.
Šegan, S., 1988. Analytical computation of atmospheric drag effects. Celestial Mech. 41, 381–388.
Sehnal, L., 1988. Thermospheric total density model TD. Bull. Astron. Inst. Czech. 39, 120–127.
Sehnal, L., 1990a. Theory of the motion of an artificial satellite in the Earth atmosphere. Adv. Space Res. 10 (3–4), 297–301.

Sehnal, L., 1990b. Comparison of the thermosphere total density model TD 88 with CIRA 86. Adv. Space Res. 10 (6), 27–31.

Sehnal, L., Pospíšilová, L., 1988. Thermospheric model TD88. Preprint No. 67 of the Astronomical Institute of Czechoslovakian Academy of Sciences.

Sehnal, L., Pospíšilová, L., 1991. Lifetime of the ROHINI A satellite. Bull. Astron. Inst. Czech. 42, 295–297.

Sterne, T.E., 1960. An Introduction to Celestial Mechanics. Interscience Publishers, New York.

Villain, J.-P., Berger, C., Barlier, F., 1979. Analysis of thermospheric density enhancement and observation of perturbations in the equatorial zone during a magnetic storm. C. Rend. Acad. Sci. Paris 289, 25–28.

Walker, R., Crowther, R., Swinerd, G.G., 1997. The long-term implications of operating satellite constellations in the low Earth orbit debris environment. Adv. Space Res. 19 (2), 355–358.

Wharton, L.E., Spencer, N.W., Mayr, H.G., 1984. The Earth's thermospheric superrotation from Dynamics Explorer 2. Geophys. Res. Lett. 11, 531–533.

Zarrouati, O., 1987. Trajectoires Spatiales. Cepaudes-Editions, Toulouse.